Preparation of Anisotropic Multiscale Micro-Hydrogels Via Two-Photon Continuous Flow Lithography

Purnima N Manghnani, Valentina Di Francesco, Carlo Panella La Capria, Michele Schlich, Marco Elvino Miali, Thomas Lee Moore, Alessandro Zunino, Marti Duocastella, Paolo Decuzzi

Journal of Colloid and Interface Science
Volume 608, Part 1, 15 February 2022, Pages 622-633

https://doi.org/10.1016/j.jcis.2021.09.094

Journal Pre-proofs

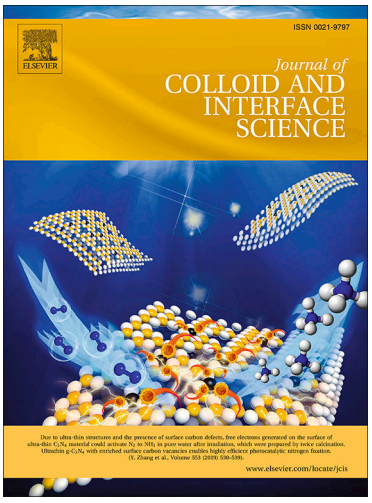

Preparation of Anisotropic Multiscale Micro-Hydrogels Via Two-Photon Continuous Flow Lithography

Purnima N Manghnani, Valentina Di Francesco, Carlo Panella La Capria, Michele Schlich, Marco Elvino Miali, Thomas Lee Moore, Alessandro Zunino, Marti Duocastella, Paolo Decuzzi

PII: S0021-9797(21)01553-8
DOI: https://doi.org/10.1016/j.jcis.2021.09.094
Reference: YJCIS 28840

To appear in: *Journal of Colloid and Interface Science*

Received Date: 15 May 2021
Revised Date: 31 August 2021
Accepted Date: 17 September 2021

Please cite this article as: P.N. Manghnani, V.D. Francesco, C.P.L. Capria, M. Schlich, M.E. Miali, T.L. Moore, A. Zunino, M. Duocastella, P. Decuzzi, Preparation of Anisotropic Multiscale Micro-Hydrogels Via Two-Photon Continuous Flow Lithography, *Journal of Colloid and Interface Science* (2021), doi: https://doi.org/10.1016/j.jcis.2021.09.094

PREPARATION OF ANISOTROPIC MULTISCALE MICRO-HYDROGELS VIA TWO-PHOTON CONTINUOUS FLOW LITHOGRAPHY

*Purnima N Manghnani, Valentina Di Francesco, Carlo Panella La Capria, Michele Schlich, Marco Elvino Miali, Thomas Lee Moore, Alessandro Zunino, Marti Duocastella, Paolo Decuzzi**

Dr. Purnima N Manghnani, Dr. Valentina Di Francesco, Carlo Panella La Capria, Dr. Michele Schlich, Dr. Marco Elvino Miali, Dr. Thomas Lee Moore and Prof. Paolo Decuzzi
Laboratory of Nanotechnology for Precision Medicine, Fondazione Istituto Italiano di Tecnologia, Via Morego 30, 16163 Genoa, Italy
* Corresponding Author: paolo.decuzzi@iit.it

Alessandro Zunino and Dr. Marti Duocastella
Nanoscopy, CHT Erzelli, Fondazione Istituto Italiano di Tecnologia, Via Enrico Melen 83, Building B, 16152, Genoa, Italy

Keywords: anisotropic soft particles, two-photon polymerization, micro-hydrogels, microfluidics

Abstract

Hypothesis

Polymeric anisotropic soft microparticles show interesting behavior in biological environments and hold promise for drug delivery and biomedical applications. However, self-assembly and substrate-based lithographic techniques are limited by low resolution, batch operation or specific particle geometry and deformability. Two-photon polymerization in microfluidic channels may offer the required resolution to continuously fabricate anisotropic micro-hydrogels in sub-10 μm size-range.

Experiments

Here, a pulsed laser source is used to perform two-photon polymerization under microfluidic flow of a poly(ethylene glycol) diacrylate (PEGDA) solution with the objective of realizing

anisotropic micro-hydrogels carrying payloads of various nature, including small molecules and nanoparticles. The fabrication process is described via a reactive-convective-diffusion system of equations, whose solution under proper auxiliary conditions is used to corroborate the experimental observations and sample the configuration space.

Findings

By tuning the flow velocity, exposure time and pre-polymer composition, anisotropic PEGDA micro-hydrogels are obtained in the 1 – 10 μm size-range and exhibiting aspect ratio varying from 1 to 5. Furthermore, 200 nm curcumin-loaded poly(lactic-co-glycolic acid) (PLGA) nanoparticles and 100 nm ssRNA-encapsulating lipid nanoparticles were entrapped within square PEGDA micro-hydrogels. The proposed approach could support the fabrication of micro-hydrogels of well-defined morphology, stiffness, and surface properties for the sustained release of therapeutic agents.

Introduction

In the context of drug delivery, various formulation strategies like liposomes, niosomes, polymeric micelles and nanoparticles have been developed and optimized for achieving biodegradability and site-specific action.[1-4] These particle formulations are typically spherical and rely on self-assembly through bulk emulsion[5, 6] or microfluidics[7, 8] for synthesis. As a result, the most studied formulation properties have been particle hydrodynamic size and surface electrostatic potential.[9, 10] More recently, the aspect ratio (AR) and mechanical stiffness of nano/micro particles are emerging as important formulation variables to fine tune biomedical performance.[11-13] Within this context, polymeric hydrogel microparticles (HMP) are garnering attention as they can be engineered into different morphologies. Moreover, hydrophilic polymers that cross-link to form the HMP allow for absorption of water leading to soft bio-mimicking constructs. The swelling ratio and therefore, deformability of the particle, can be controlled by altering the polymer molecules or the cross-

linking density. For instance, Merkel et al. studied the effect of red blood cell-mimicking HMP deformability on blood circulation and correlated an 8-fold decrease in HMP elastic modulus to a 30-fold increase in the circulation half-life.[14] In addition, complex particle morphologies with high aspect ratios can evade phagocytosis by macrophages. This has been attributed to the inability of macrophages to form the necessary actin structures for phagocytosis of anisotropic particles.[12, 15] Moreover, red blood cell mimicking particles can localize preferentially in different equilibrium positions within the blood stream affecting how they interact with the endothelial cells and partition between the macro and micro-circulation.[16-20]

Numerous methods such as imprint lithography,[19-21] particle replication in non-wetting templates,[22] PVA film stretching,[23] and nanoimprint lithography[24] have been explored for anisotropic particle synthesis. These methods are however, limited by low resolution, batch operation or specific particle geometries. In this regard, continuous flow photolithography (CFL)[25] in microfluidic channels offers advantages like continuous synthesis, economic feasibility and wide range of particle geometries. Conventionally, CFL involves photopolymerization of a pre-polymer in a poly(dimethylsiloxane) (PDMS) microfluidic chip by subjecting it to ultraviolet (UV) light stimulus. Although HMP of size $>$ 20 μm and varied geometries have been developed using microfluidic systems, particles in the 1 – 10 μm size range remain largely unexplored. Complex geometries of smaller size have been achieved by using high-resolution illumination like a two-photon light source.[26, 27] In two-photon polymerization (2PP), an ultrashort infrared laser pulse focused through a lens initiates free radical polymerization in the focal volume. This approach has been demonstrated in photoresists flowing through microfluidic channels since they allow for flow rates conducive for continuous 2PP and obviate the need of a piezo stage. However, these endeavors have mainly focused on developing complex particle geometries in a microfluidic stream with

movable mirrors.[26, 28] Furthermore, it remains to be demonstrated that the so-fabricated particles can be rendered functional by incorporating diverse payloads.

In this work, using simple 2PP in a microfluidic channel, poly(ethylene glycol) diacrylate (PEGDA) anisotropic multiscale micro-hydrogels (MMH) have been fabricated in the size range of 1 – 10 μm with varied aspect ratios and different payloads, including small molecules, liposomes and polymeric nanoparticles. While most of the 2PP studies focus on reducing the anisotropy of the beam spot to print 3D structures, here authors take advantage of the inherent asymmetry of the Gaussian femtosecond-laser beam to fabricate anisotropic MMH. It is shown that the MMH aspect ratio (AR) can be tuned by controlling the shutter frequency, flow rate and resist composition. Furthermore, a computation model is developed to corroborate the experimental results and define the parameter space in which the 2PP system can be operated to get MMH with a specific geometry.

Experimental Section

Microfluidic device:

Microfluidic devices were fabricated by pouring polydimethylsiloxane (PDMS, Sylgard 182, Dow Corning) in 9:1 w/w base to curing-agent ratio on a silicon wafer containing positive-relief channels patterned in SU-8 photoresist, and by thermal curing at 80 °C for 2 hours. The microfluidic channel was of length (x) 15 mm, height (z) 40 μm and width (y) 200 μm. Devices were fabricated by cutting out the PDMS channel using a razor blade, punching holes at the inlet and outlet for the fluid. The PDMS devices were then plasma sealed to glass slides by subjecting them to oxygen plasma (30 s at 30 W). The inlet was connected to a syringe driven by a syringe pump using flexible silicone tubing and particle were collected using a pipette tip at the outlet.

Materials:

The pre-polymer solution consists of poly(ethylene) glycol diacrylate (PEGDA, Mn = 700, Sigma Aldrich), Lucirin TPO-L (ethyl-2,4,6-Trimethylbenzoylphenylphosphinate, Fluorochem) as the two-photon free radical photoinitiator (PI) and DI water. The MMH were developed in 70 % vol ethanol. Since Lucirin TPO-L is insoluble in water, for nanoparticle cargo sensitive to ethanol treatment, 6 mM lithium phenyl-2,4,6-trimethylbenzoylphosphinate (LAP) from Sigma Aldrich was used as the PI so that the MMH could be developed in water. For LAP PI, the system was operated at 60 mW pre-objective. For fluorescence labeling the polymer, 0.005% wt of methacryloxyethyl thiocarbamoyl rhodamine B (Sigma Aldrich) was added to the pre-polymer solution.

For nanoparticle loading, 200 nm Rhodamine labelled polystyrene beads (Fluoresbrite Carboxy NYO Polyscience Inc.) were added at a concentration of 14.4×10^8 particles/mL.

For the Curcumin SPNs, Poly(lactic-co-glycolic acid) (50:50, Carboxy-terminated, MW 38,000–54,000 Da) was purchased from Sigma Aldrich (St. Louis, MO, USA). 1,2-dipalmitoyl-sn-glycero-3-phosphocholine (DPPC) and 1,2-distearoyl-sn-glycero-3-phosphoethanolamine-N-[Carboxy(Polyethylene Glycol)-2000] (DSPE-PEG) were obtained from Avanti Polar Lipids (Alabaster, Alabama). Curcumin (95% total curcuminoid content) was purchased from Alfa Aesar. Chloroform, Acetonitrile and other solvents were obtained from Sigma Aldrich.

For the FAM LNPs, 1,2-dioleoyl-3-dimethylammonium-propane (DODAP), 1,2-dipalmitoyl-sn-glycero-3-phosphocholine (DPPC), 1,2-distearoyl-sn-glycero-3-phosphoethanolamine-N-[methoxy(polyethylene glycol)-2000] (DSPE-PEG2k) were purchased from Avanti Polar Lipids Inc (Alabaster, AL). Cholesterol was purchased from Merck. FAM-labeled single-stranded RNA was synthesized by Integrated DNA Technologies (5'-6FAM-UCGUUAAUCGGCUAUAAUACGC-3').

Bulk gel fabrication and porosity/swelling measurements:

PEGDA bulk gels were synthesized with four formulation combinations from varying PEGDA between 65 and 95 vol % and PI between 2 and 5 vol %. The polymerization was carried out in microwells of 0.75 cm diameter, holding 50 µL of pre-polymer. The microwells were subjected to 15 seconds of polymerization under a UV lamp (365nm, 2 × 15W) at distance of 2 cm. The resulting gels were ejected from the mold using a syringe needle and washed in ethanol and water. The hydrogel discs were dried under vacuum overnight and were weighed immediately (m_{dry}). The discs were soaked in excess ethanol for 2 days. The wetted hydrogels were retrieved, the excess ethanol was wicked from surface using kimwipes and were weighed (m_{EtOH}). The porosity was calculated according to the formula

$$Porosity\ \% = \frac{(m_{EtOH} - m_{dry}) \times 100}{\rho_{EtOH} V}$$

where V is the volume of the swollen sample. The swelling ratio of the bulk gels were obtained by soaking the dry gels in water for 2 days. The wetted hydrogels were retrieved, the excess water was wicked from surface using kimwipes and were weighed (m_{wet}). The swelling ratio was calculated according to the formula

$$Swelling\ ratio = \frac{m_{wet} - m_{dry}}{m_{dry}}$$

Particle fabrication:

The fluid velocity of the pre-polymer solution was varied between 100 µm/s and 150 µm/s. The fs laser beam was directed into the 63 × 1.4 NA objective through a dichroic mirror housed in an Olympus Fluoview FV 1000 microscope. The optical shutter (Thor Labs MC1F10 10-slot) was operated at set points of 30 and 60 Hz to vary particle width. As the polymerization occurred in the focal spot, a CCD camera was used to visualize the polymerization in real time. Once the particles were collected, they were developed in 70 % ethanol solution and centrifuged for 30 minutes at 3900 rpm to collect them. Rhodamine B acrylate, PS beads, SPNs, Cy5 Liposomes and FAM LNPs were added to the pre-polymer for fluorescent labeling and drug

encapsulation during MMH fabrication. For MMH encapsulating LNPs and liposomes, they were developed in water and therefore were separated using centrifugation using Amicon Ultra-4, Centrifugal Filter 10,000 Da.

MMH characterization:

MMH concentration and size distribution profiles were performed through Multisizer (Beckman Coulter, USA). Fluorescence microscopy (Leica 6000) was used to acquire fluorescent images of the particles. Scanning Electron Microscopy (SEM) (JEOL, Japan) was used for morphological analysis of MMH. The sample were prepared by the drop casting method over glass cover slips. The samples were sputtered with 10 nm of Gold and analyzed operating at an acceleration voltage of 10 kV. Confocal images of particle were obtained using an A1-Nikon confocal microscope (Nikon Corporation, Japan). Transmission Electron Microscopy (TEM) (JEOL, Japan) images were also used to characterize the MMH.

SPN and LNP synthesis and characterization:

SPN were synthesized by employing an emulsion/solvent evaporation technique. DSPE-PEG was dissolved in a 4% ethanol solution to a final volume of 3 ml to obtain the aqueous phase, whereas 1 mg of PLGA and an appropriate quantity of DPPC were dissolved in chloroform to create the oil phase. A v/v ratio of 6:1 between the aqueous and organic phase, a lipids/polymer w/w ratio of 20% and a DPPC/DSPE-PEG molar ratio of 7.5:2.5 were used. Then, the oil phase was added in a dropwise manner to the aqueous solution under ultrasonication at 60% amplitude (Q125 sonicator, Q-Sonica). The resulting emulsion was then gently stirred at room temperature and in a reduced pressure environment for 4 h to allow solvent evaporation. Finally, nanoparticles were washed with water by centrifugation at 1,500 rpm for 5 min to remove any possible debris obtained in the synthesis process. The nanoparticles solution was then centrifuged at 12,700 rpm for 20 min and the pellet was resuspended in 100 μL of Milli-Q water.

SPN size and polydispersity index (PdI) were estimated by dynamic light scattering (DLS) using Malvern Nano-ZS Zetasizer diluting 5 µl SPNs in 1000 µl deionized water.

Cy-5 containing liposomes were synthetized by thin layer evaporation (TLE). Briefly DPPC, cholesterol, DSPE-PEG and DSPE-Cy5 were dissolved in chloroform in a round bottomed flask (ratio 6:3:1:1). The thin layer lipid film was obtained with the evaporation of the organic solvent at 60 °C under reduced pressure using a Rotovapor. Then, it was left under the hood overnight to remove any trace of residual solvent. For the production of the multilamellar liposomes, the lipid film was hydrated with 2 mL of HEPES and then subjected to three alternate cycles (3 min each) of warming at 60 °C (thermostated water bath) and vortexing at 700 rpm. The purification step to remove excess of Cy-5 was conducted by ultracentrifugation (1h, 45,000 rpm) instead of dialysis.

LNP were prepared by microfluidic mixing using a Nanoassemblr Benchtop (Precision NanoSystems, Vancouver, BC). Briefly, one volume of a DODAP, DPPC, cholesterol, DSPE-PEG2k (50/10/38.5/1.5 mol ratio) solution in ethanol was rapidly mixed four volumes of FAM-labeled RNA dissolved in citrate buffer (pH 3.9) at a total flow rate of 2 ml/min (0.019 w/w RNA/lipid). The obtained LNP were dialyzed for 16 h against PBS pH 7.4 and concentrated by centrifugal ultrafiltration units (Amicon Ultra 4, 30kDa MWCO, Millipore) to a final RNA concentration of 0.266 mg/ml. The mean diameter and PdI of LNPs were measured by DLS using a Malvern Nano-ZS Zetasizer (Malvern, Worcestershire, UK), diluting 5 µl LNPs in 500 µl deionized water.

Predicting the MMH geometry:

We devised a two-dimensional model to describe the linear non-steady state process of MMH formation in continuous flow. We limited our problem to the xz space where z is the optical axis and x is the flow direction. The photo-polymerization occurred in the center of a

rectangular PDMS channel, far away from the channel walls. The reaction scheme is shown in **Table 1**.

No.	Reaction	Mechanism
1	$P \rightarrow 2\,R\cdot$	Photolysis
2	$R\cdot + M_n \rightarrow R\cdot$	Initiation and propagation
3	$R\cdot + R\cdot \rightarrow R_{dead}$	Termination
4	$R\cdot + O_2 \rightarrow R_{dead}$	Inhibition

Table 1: 2PP reactions

We assume that the photoinitiator molecule *P* absorbs only two photons of light to cleave into free radicals $R\cdot$, neglecting possible multiphoton pathways. The free radicals react with the monomer molecules M_n to generate a chain-initiating radicals $RM\cdot$. These radicals further propagate the polymerization. For simplicity, we consider the $RM\cdot$ radicals analogous to $R\cdot$. The first mode of termination occurs when two active radicals combine, and the second mode of termination occurs when the dissolved oxygen inhibits the radical propagation. In this model, only bimolecular termination was considered, while other modes of termination such as the trapping of radical species were neglected. The intensity distribution of laser beam was approximated as a Gaussian beam of intensity $I\,(x,z)$ that can be expressed as:

$$I\,(x,z) = I_o\left(\frac{\omega_o^2}{\omega^2(z)}\right)e^{-2x^2/\omega^2(z)} \tag{1}$$

$$\text{Where } I_o = 2.3\,I_{focus}\,,\ I_{focus} = \frac{P}{\pi\omega_o^2\tau F} \text{ and } \omega_o = \frac{\lambda}{\pi\,NA} \tag{2}$$

where I_o is the laser intensity at the beam center, *P* is the average power, *F* is the laser repetition rate, τ is the laser pulse width, ω_o is the beam waist and $\omega(z)$ is the beam radius in the channel at a distance z. $\omega(z)$ can be expressed as follows:

$$\omega(z) = \omega_o\sqrt{1 + \left(z/z_R\right)^2} \tag{3}$$

z_R is the Rayleigh length given by,

$$z_R = \frac{\pi n \omega_o^2}{\lambda} \quad (4)$$

where n is the refractive index of the polymer precursor.

Mass balance equations for this system must account for the convection, diffusion and reaction of the species. Since the length of the channel is much greater than the width and height, axial diffusion (in x-direction) can be neglected for all species. The pre-polymer solution travels through the channel at a velocity u_x. Although the velocity in a rectangular microfluidic channel for a Newtonian fluid has a plug flow profile, since the laser spot was confined to the center of the channel, we assumed a uniform velocity profile in the polymerization area (PA).

For the mass balance equation of the PI molecules, we neglected the diffusion component of the PI molecules. This assumption was considered valid because the polymerization occurred far away from the channel walls in the bulk flow and the PI molecules have a relatively large size. The mass balance for the PI molecules (P) can be written as:

$$\frac{\partial P\,[x,z,t]}{\partial t} = -u_x\left[\frac{\partial P}{\partial x}\right] - \delta\gamma F\tau P\varphi^2 \quad (5)$$

where δ is the PI two-photon cross-section, γ is the PI quantum yield and $\varphi = I/h\upsilon$, where h is the Planck's constant and υ is the light frequency. The rate of generation of radicals (R) depended on the convection and reaction terms accounting for generation and termination. Similar to PI, we neglected the diffusive component of the radical mass balance equation.

$$\frac{\partial R\,[x,z,t]}{\partial t} = -u_x\left[\frac{\partial R}{\partial x}\right] + \delta\gamma F\tau P\varphi^2 - k_t R^2 - k_{t,O_2} RO_2 \quad (6)$$

The rate of consumption of monomer (M) depended on the convection and the reaction term for the propagation of polymerization.

$$\frac{\partial M\,[x,z,t]}{\partial t} = -u_x\left[\frac{\partial M}{\partial x}\right] - k_p RM \quad (7)$$

Lastly, the rate of oxygen consumption depended on the diffusion, convection and the reaction term for the radical inhibition. The oxygen molecule has a small size and its diffusion could play a role in the 2PP. The Peclet number (*Pe*) is a dimensionless number that compares the

relative contribution of diffusion and convection of species in a process. It is defined as the ratio of the convective flux to the diffusive flux given by $u_x H/D$ where H is the channel height and D is the diffusion coefficient. For a stationary droplet, the oxygen diffusion plays a role in determining the polymerization volume. However, the *Pe* for the oxygen transport in the microfluidic channel was calculated to be in the order of 100. We further compared the PA height in case of polymerization inhibited by both convection and diffusion to polymerization inhibition by convection alone at u_x 50 μm/s. As seen in **Table S1**, the polymerization height varies at a maximum of 1.3 % under the two scenarios. Therefore, under flow conditions, we neglected the diffusive flux of oxygen species in the PA all together.

Under pure diffusion conditions, (u_x= 0)

$$\frac{\partial O_2[x,z,t]}{\partial t} = D_{O_2}\left[\frac{\partial^2 O_2}{\partial z^2}\right] - k_{t,O_2} R O_2 \tag{8}$$

under pure advection conditions,

$$\frac{\partial O_2[x,z,t]}{\partial t} = -u_x\left[\frac{\partial O_2}{\partial x}\right] - k_{t,O_2} R O_2 \tag{9}$$

The values of the rate constants were taken from the literature (**Table S2**) and the beam peak intensity was approximated for average beam powers of 5, 10 and 20 mW. We also assumed that the temperature was constant and there were no radical losses between the pulses. The equations were solved numerically with *Wolfram Mathematica®12* using method of lines on the *NDSolve* PDE solver. The simulations were run on a two-dimensional domain of 120 μm × 120 μm with the focal spot in the center of the domain. The initial and boundary conditions of the problem were defined as:

$$P[x, z, 0] = P[-x_i, z, t] = P_i$$

$$R[x, z, 0] = R[-x_i, z, t] = 0$$

$$M[x, z, 0] = M[-x_i, z, t] = M_i$$

$$O[x, z, 0] = O[-x_i, z, t] = O_i$$

where P_i, M_i and O_i signified the concentrations of the species at $t = 0$ and at the inlet face of the domain at $x_i =$ - 60 μm. The polymerization dynamics were studied for a maximum time of 64 ms as the shutter frequency used in the experimental settings led to an exposure time of a similar order.

Results and Discussion

Fabricating MMH via Continuous Flow Lithography

Micron-sized polymeric hydrogels were realized using a continuous flow lithography approach. **Figure 1a** shows a schematic representation of the fabrication set-up including an 800 nm femtosecond-laser (100 fs, 80 MHz); an optical chopper (20 – 1,000 Hz); a 63× objective (NA 1.4); a CCD camera; and a microfluidic device connected via proper tubing to a syringe pump. The microfluidic (μF) device consists of a 15 mm long, straight channel with a 200 × 40 μm rectangular cross-section realized in polydimethylsiloxane (PDMS) and sealed with a glass slide. A working solution comprising the water soluble monomer of poly(ethylene glycol) diacrylate (PEGDA), at the concentration C_{PEG}, mixed with a photoinitiator (PI), at the concentration C_{PI}, and the payload was infused in the microfluidic channel at a specific flow velocity Q using a syringe pump.

MMH were continuously fabricated by exposing the working solution to the laser beam (20 mW pre-objective) directly focused in the center of the microfluidic device (20 μm from the channel bottom). This induced the generation of PI radicals within the laser focal point that would react with the PEGDA monomers favoring the progressive and localized photopolymerization of the flowing working solution. Notice that the absorption of two photons by a PI molecule takes place in a very short time interval for radical formation, typically in sub-femtosecond range and has a quadratic dependence on the laser intensity. Subsequently, polymerization initiates when the radical concentration crosses a certain threshold. This enables

sub-diffraction limited resolution of fabricated features in both the lateral and axial directions. The optical chopper, operated at the frequency *f*, served to interrupt the solution exposure and thus realize particles with a finite size rather than a continuous line. Due to the altered refractive index, the resulting MMH could be readily observed using a CCD camera. Representative pictures of the micro-hydrogels generated within the working flow are shown in **Figure 1b**, under different conditions (continuous line – $f = 0$ Hz; distinct microparticles: $f > 0$ Hz). The full movie is available as **Supplementary Video 1**.

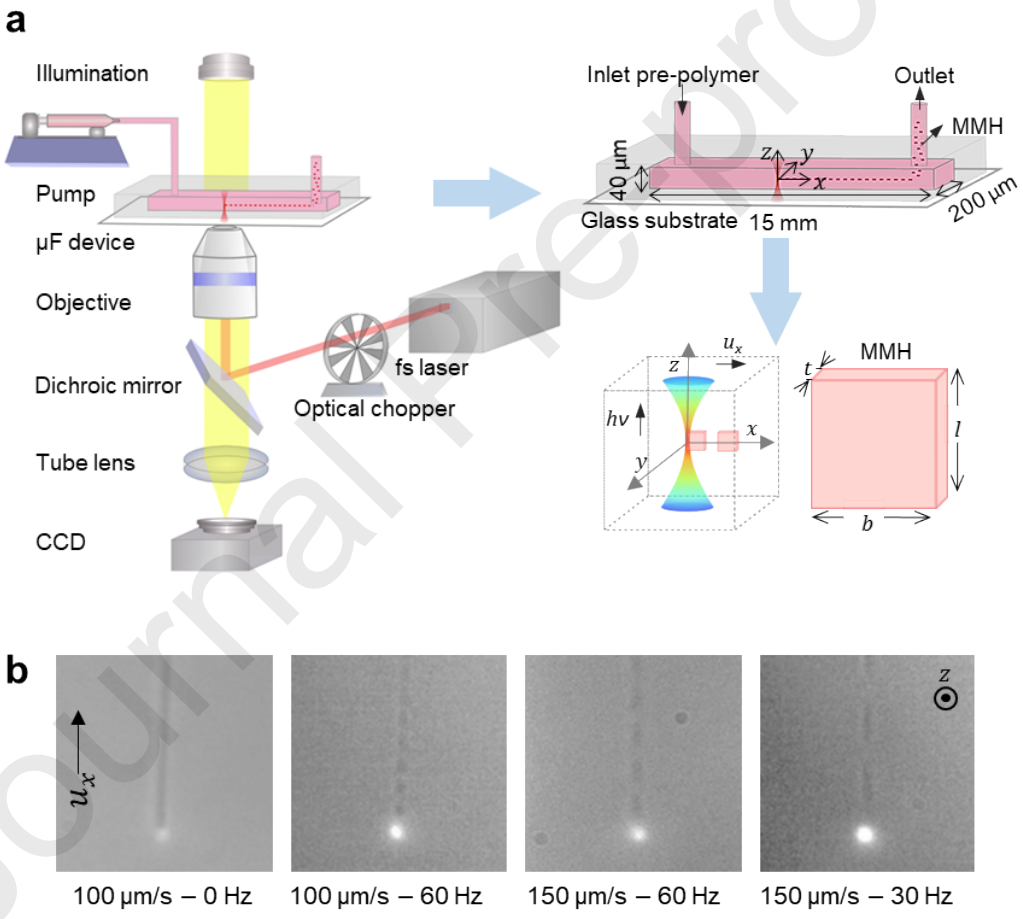

Figure 1: Fabricating MMH via Continuous Flow Lithography. a. Experimental set-up for 2PP in a microfluidic channel and schematic depicting MMH formation and dimensions (length – l, width – b and thickness – t). **b.** Snapshots of MMH fabrication at different operating conditions.

More specifically, referring to a cubic volume surrounding the laser spot (**Figure 1a**), MMH were continuously produced in the fluid flow direction *x* returning thin cylinders with a width *b*, along the *x*-direction aligned with the flow; a length *l*, in the *z*-direction normal to the flow and aligned with the laser beam; and a thickness *t*, in the y-direction normal to the flow. The MMH width *b* is mostly governed by the distance travelled by the fluid volume in the *x* flow direction while being exposed to the laser beam. Consequently, *b* can be tailored by controlling the flow rate *Q* and the chopper frequency *f* (exposure time). Due to the asymmetry of the laser beam spot (**Figure S1**), the length *l* of the MMH is determined by the intensity distribution along the optical axis *z*. The Gaussian laser beam focused into the monomer is asymmetric in the *xz* plane and symmetric in the *xy* plane. The laser intensity in the *xy* plane is tightly focused by virtue of a high NA objective, therefore the resulting MMH thickness *t* was in the sub-micrometer scale.

Modulating the MMH geometry

The geometry of the MMH can be tailored by controlling multiple operating parameters including the flow velocity *Q* of the working solution; the working frequency *f* of the optical chopper; the concentrations of PEGDA C_{PEG} and of the photo initiator C_{PI}; the laser intensity *I*; and the geometry of the channel. In this work, the MMH geometry was systematically modulated by working at two different flow velocities, namely *Q* equal to 100 μm/sec and 150 μm/sec; two chopper frequencies, namely *f* equal to 30 and 60 Hz; and considering two PEGDA and PI concentrations, being C_{PEG} equal to 65 and 95 vol% and C_{PI} 2 and 5 vol% respectively. Scanning Electron Microscopy images of MMH with different geometries are presented in **Figure 2**.

As the frequency *f* of the optical chopper increases from 30 to 60 Hz, the working fluid is exposed to the laser beam for a shorter period (from 33.3 to 16.6 ms). As a result, the width *b* of the MMH reduces. For instance, the width of MMH reduced by about a factor of two, from

b = 2.21 ± 0.09 to 1.15 ± 0.13 μm, as f increased from 30 to 60 Hz (Q = 100 μm/s, C_{PI} = 5 vol% and C_{PEG} = 95 vol%). Note that such a significant change in width was accompanied by only a 4% decrease in length l of the MMH, from l = 6.50 ± 0.22 to 6.21 ± 0.13 μm. Alternatively, changing the flow rate Q from 100 to 150 μm/s while keeping f constant causes more working fluid to be exposed to the laser beam. Thus, an increase in the width b of the MMH was observed. Specifically, as Q increased from 100 to 150 μm/s (f = 30 Hz; C_{PI} = 5 vol% and C_{PEG} = 95 vol%), the width of MMH increased by about 28%, from b = 2.21 ± 0.09 to 2.84 ± 0.15 μm, and the length decreased by 22%, from l = 6.50 ± 0.22 to 5.02 ± 0.09 μm.

Differently from Q and f, the concentrations of the monomer PEGDA and photoinitiator PI have a predominant effect on the length l of the MMH. For instance, increasing C_{PEG} from 65 to 95 vol% resulted in a longer MMH with l increasing by 20% at lower flow rates, and 14% at higher flow rates. A similar trend is observed for C_{PI}. For instance, increasing C_{PI} from 2 to 5 vol% resulted in a longer MMH with l increasing by about 22%, at both low and high flow rates. Following a decrease in C_{PEG} and C_{PI}, the width b of the MMH is also reduced by ~ 15% and 10%, respectively – a change significantly smaller than for l. Such an effect can be explained by considering that, for a fixed flow rate Q and optical chopper frequency f, the volume of working fluid exposed to the laser beam along the flow direction (x-direction coincides with the particle width b) does not change. However, increasing the concentration of PEGDA and PI facilitates the photopolymerization especially in the laser direction (normal to the flow) thus resulting in longer particles. This becomes less evident as the time available for polymerizing a single MMH reduces or, in other words, as the flow rate increases as convection tends to dominate over diffusion. Apart from this, change in pre-polymer composition could affect the cross-linking density of the MMH leading to different porosity. The porosity and swelling ratio of bulk PEGDA hydrogels with identical pre-polymer concentrations was investigated. For a given excitation energy, both C_{PEG} and C_{PI} were found to affect the porosity and swelling ratio

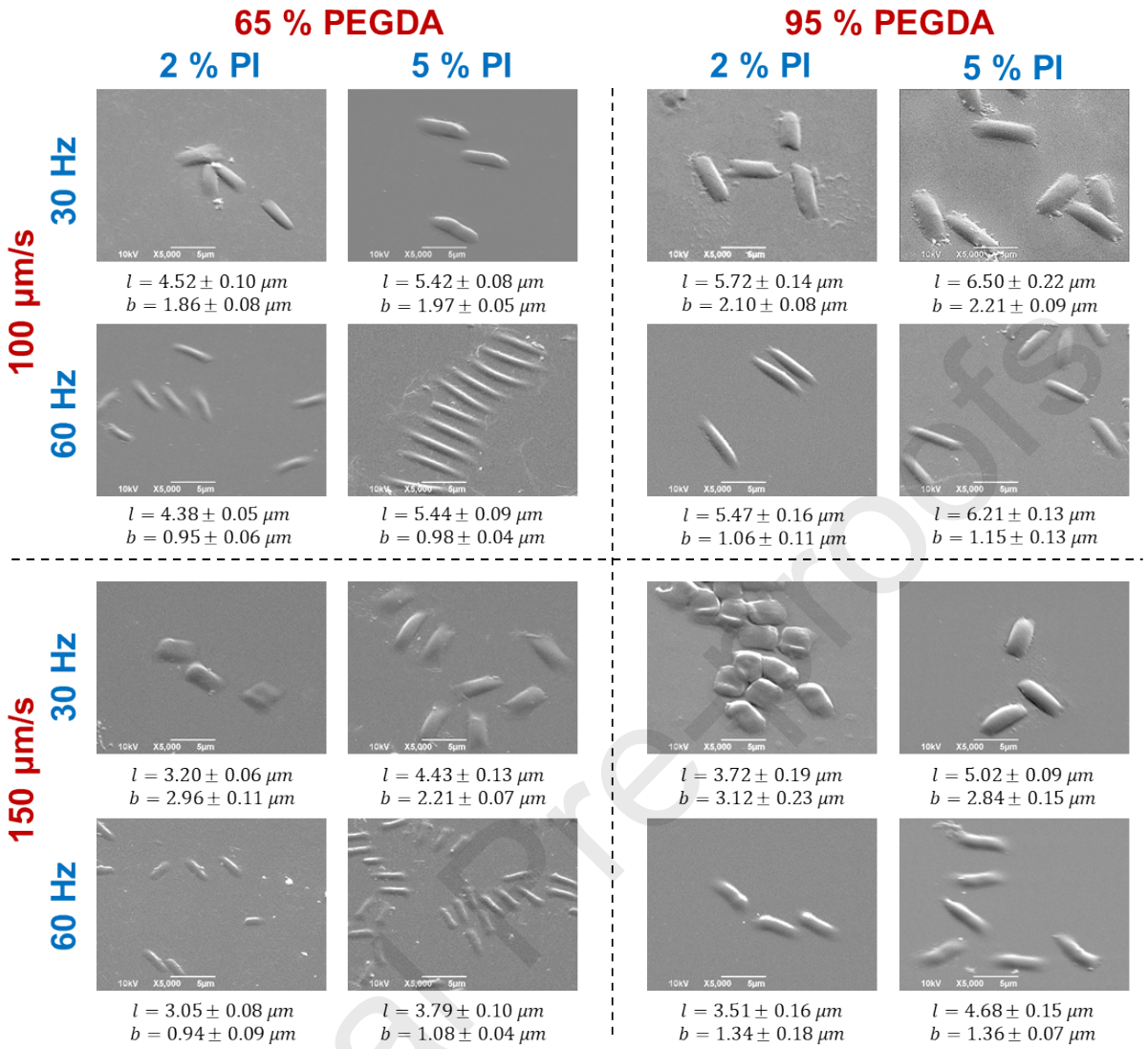

Figure 2: **Morphological characterization of MMH.** Scanning Electron Microscopy images of MMH fabricated by varying fluid velocity (100 – 150 µm/s), shutter speed (30 – 60 Hz), PEGDA volume percentages (95 – 65%) and PI volume percentages (2 – 5%).

(Figure S2) of the resulting bulk gels. A decrease in both C_{PEG} and C_{PI} led to an increase in porosity and swelling ratio. This phenomenon could further contribute to the size difference of the MMH in dry conditions.

Predicting the MMH geometry

The polymerization process of MMH under flow can be described as an advection-diffusion-

reaction problem defined by a set of differential equations documenting the variation in

concentrations of the different reactive chemical species (PEGDA monomer, PI, and payload) in space and time. **Table 1** schematically presents the multiple reaction steps and chemical species involved in the polymerization process, while the full set of governing equations with

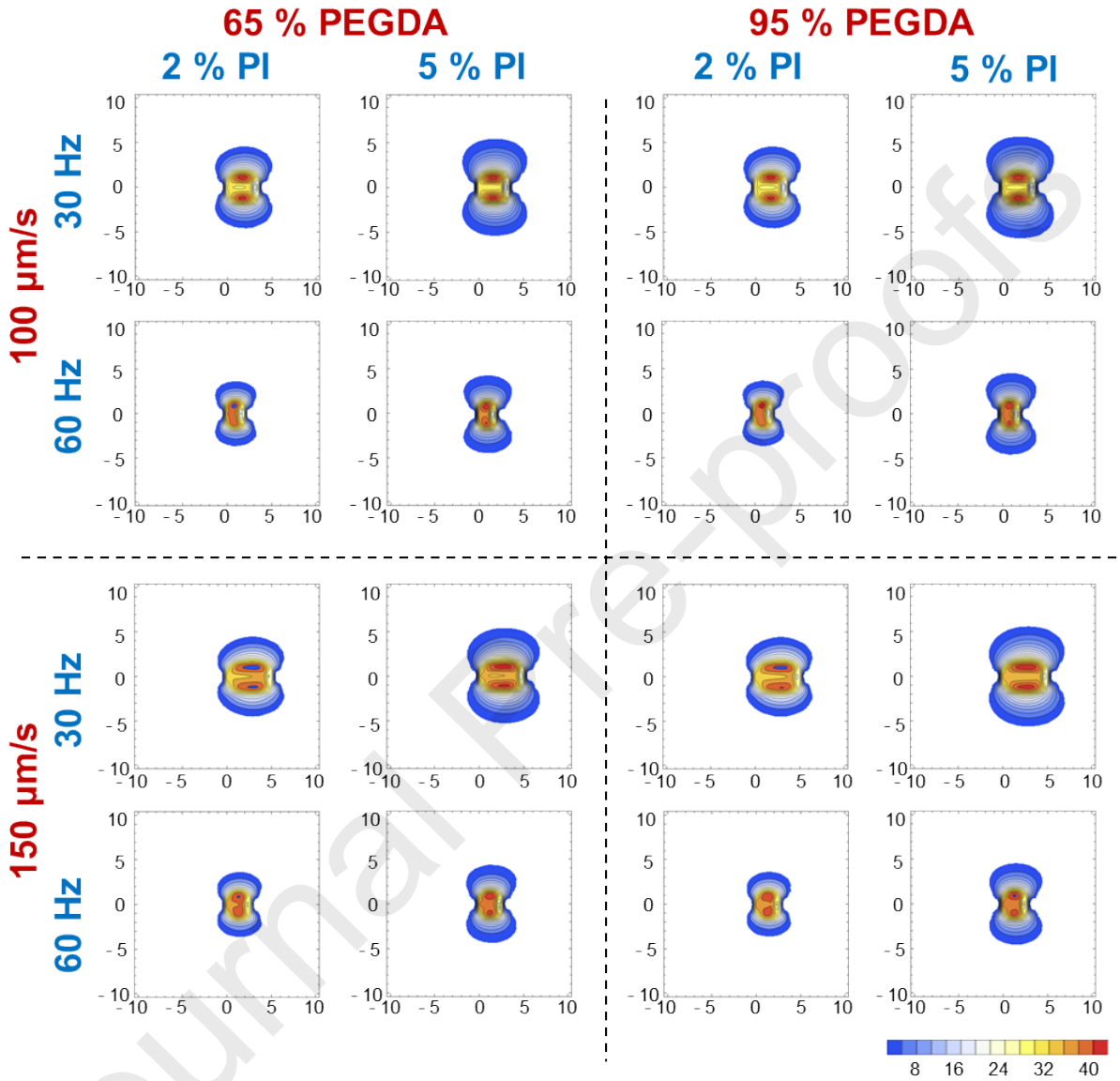

Figure 3: **Predicted extension of the polymerization area (PA) under different operating conditions.** Contour plots for the concentration of polymerized PEGDA (polymerization area – PA) for varying fluid velocity, shutter speed, PEGDA and PI volume percentages, at 20 mW laser power. The boxes are ($x \times z$) 10 µm × 10 µm. The legends depict the percentage of PEGDA conversion into polymer. External to the blue area, the polymerization is lower than 2% indicating no gel formation. The width *b* and length *l* of the MMH correlate with the base and height of the PA in the contour plots above.

proper boundary and initial conditions are provided in the **Experimental** section. It should be here recalled that although various groups have developed computational models for 2PP, these describe the polymerization in a static droplet exposed to the laser beam therefore, accounting only for diffusive and reactive processes.[29, 30] In this article, convective terms for the flowing monomer in the microfluidic channel have been included to provide a more comprehensive description.

The integration of the boundary value problem allowed the authors to predict the extension of the polymerization area (PA), which could be correlated with the MMH geometry, under different operating conditions. Assuming that PEGDA molecules cross-link to form a solid MMH upon 2% conversion,[31] **Figure 3** gives the actual contour within the *xz* plane of the PA: all the points within the blue area are associated with a polymerized gel (polymerization > 2%), whereas all the points outside the blue area received an insufficient amount of energy to form a gel structure (polymerization < 2%). From these contour plots, the width *b,* in the flow direction *x*, and length *l*, in the laser direction *z*, of the PA can be extrapolated. These two geometrical parameters can be calculated as a function of the laser intensity *I*, flow velocity *Q*, chopper frequency *f*, PEGDA and PI concentrations C_{PEG} and C_{PI}. By comparing **Figure 2** and **3**, it can be readily appreciated that an increase in flow velocity *Q* (or decrease in chopper frequency *f*) is associated with an increase in the width *b* of the PA (particle size in the flow direction *x*); while an increase in PEGDA and PI concentrations is responsible for an enlargement of the overall polymerization area, and especially in the length *l* (particle size in the laser beam direction z).

A more detailed analysis of the effect of these four major governing parameters on the particle geometry is provided in **Figure 4**. First, the effect of the fluid velocity *Q* is shown in **Figure 4a**. The PA width *b* is associated with the dashed lines, whereas the PA length *l* is given by the solid lines. The line colors are related to the laser power, varying from 5 mW (black) to 10 mW (blue) and to the experimental value of 20 mW (red). It is confirmed that the PA width *b* grows

with Q returning a quasi-linear relationship with a coefficient of proportionality close to unity. This is indeed consistent with the data of **Figure 2**, particularly for low shutter frequencies and low C_{PI}. In the same **Figure 4a**, it is also shown that the PA length l decreases with Q. Interestingly, the laser power has a major effect on the PA length l only: the higher the laser power, the higher the PA length. This is consistent with the general observation that the particle width b is mostly governed by flow and shutter frequency f, whereas the particle length l is mostly affected by the polymerization process per se. **Figure 4b** shows the variation of the PA size under static conditions (pure diffusion with no advection – Q = 0 μm/sec) for different values of the laser power I (= 5, 10 and 20 mW) and frequency f of the optical chopper, ranging from 16 to 400 Hz. The plot shows that the PA length l increases as the frequency f decreases (larger exposure time), as polymerization proceeds along the laser direction. However, upon longer exposure times (~100 ms or f < 10 Hz), the PA length growth slows down due to oxygen depletion in the area of polymerization and therefore, oxygen diffuses from the surrounding fluid (**Figure S3**). This might point to the possibility that at 30 Hz, the oxygen diffusion does not affect the PA length significantly. Furthermore, the PA generated at 30 Hz in a stationary droplet was compared to that generated under advection/diffusion conditions with Q = 100 μm/s (**Figure S4**). An increase in PA width and decrease in PA length was recorded between the two conditions, confirming that advection does affect the MMH length. As seen in **Figure 3**, at a laser power of 20 mW the fluid velocity and chopper frequency directly influenced the PA width. Meanwhile the flow velocity also affected the PA length. This could be attributed to the competition of advection and reaction in the PA. This is even more relevant at lower laser power for which the stagnation point moves toward larger chopping frequency values.

As the PI concentration increases, the PA length *l* increases too as documented in **Figure 4c**. The effect of the PEGDA concentration, however, was found to be tied to the PI concentration. Furthermore, at low PI concentration of 2 vol%, change in PEGDA concentration did not seem to affect the PA. At higher PI concentration, the increase in PEGDA concentration led to an increase in the PA height. This could be attributed to the high cross-linking ability of the PEGDA molecules and therefore, the limiting factor in MMH formation would be the number of radicals generated by the PI. The effect of the fluid velocity on the PA length as the exposure time increases is shown in **Figure 4d-f**. It is interesting to note that at higher laser intensities, the PA length *l* continues to grow with time sharply compared to the lower beam intensities

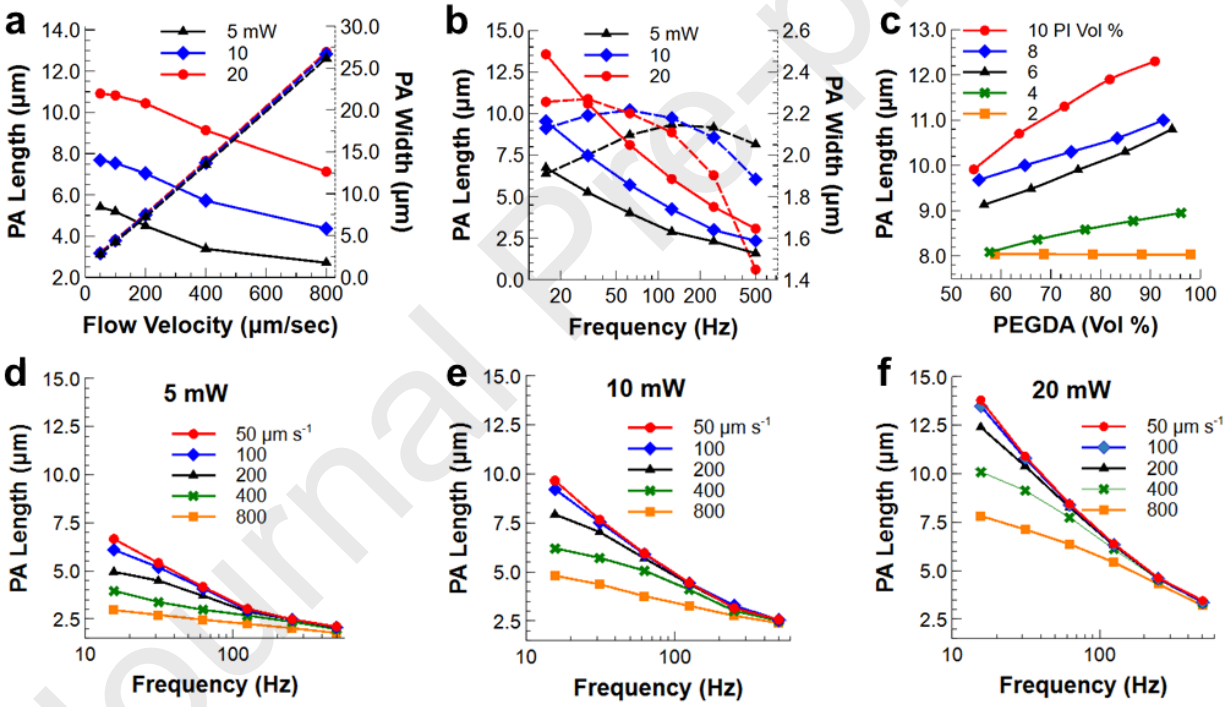

Figure 4: **Predicting the PA geometry. a.** Variation of simulated PA length (solid line) and width (dotted line) in flowing pre-polymer with flow velocity and laser power at 30 Hz. **b.** Variation of simulated PA length and width in a static droplet with frequency for different peak laser power. **c.** Variation of simulated PA length with changing PEGDA and PI concentrations at 20 mW, 100 μm/s. **d-f.** Profiles of PA length development with varying flow rates and laser power.

where the PA length growth follows a relatively flat profile. Overall, from these results, the effect of the operating parameters in the fabrication process on the PA, and therefore MMH geometry, could be confirmed.

MMH with different aspect ratios

Starting from the observations above, MMH with three distinct geometries were realized, namely needle-shaped MMH with an aspect ratio AR ~ 5; rectangular MMH with AR ~ 3 and square MMH with AR ~ 1. These were further characterized using a Coulter Counter multisizer apparatus returning the size distribution profiles presented in **Figure 5a**. Given the non-spherical and highly non-isotropic geometry of the needle shaped MMH, the distribution curve returns an average size of 1.98 ± 0.13 μm which is an intermediate value between the particle length l = 5.74± 0.11 μm and width b = 1.13 ± 0.05 μm. For the less elongated rectangular MMH, the Coulter Counter multisizer returned an average size of 2.53 ± 0.24 μm which is again comprised between the particle length l = 4.30 ± 0.16 μm and the width b = 1.47 ± 0.07 μm. Finally, for the more isotropic square MMH, the instrument provided an average size of 3.37 ± 0.27 μm which is quite close to the edge size l = b ~ 3.43 ± 0.10 μm, as form the SEM images presented in **Figure 5b-d (left column)**. The three MMH geometries were also characterized using TEM (**Figure S5**). To visualize the particle geometry and demonstrate the ability of MMH to carry a payload, the hydrophilic fluorescent molecule RhB-acrylate was dispersed in the working solution together with the PEGDA monomer. Upon polymerization, the RhB-acrylate was crosslinked directly with the monomers becoming part of the resulting MMH structure. Fluorescence confocal microscopy images of the three different MMH types are provided in **Figure 5b-d (right column)**. Notice that the MMH exhibited an uneven fluorescent signal distribution along their structure, with a minimum in intensity at the particle center (**Figure S6**). This has to be attributed to the high photon flux at the laser beam waist (see **Figure S1**) causing RhB quenching, as previously documented by other authors [28].

Incorporating a payload into MMH

In the previous paragraph, it has been shown that the cross-linkable fluorophore RhB-acrylate can be mixed with PEGDA and the PI in the same working solution and generate red fluorescent MMH. Following the same approach other payloads can be readily distributed and incorporated

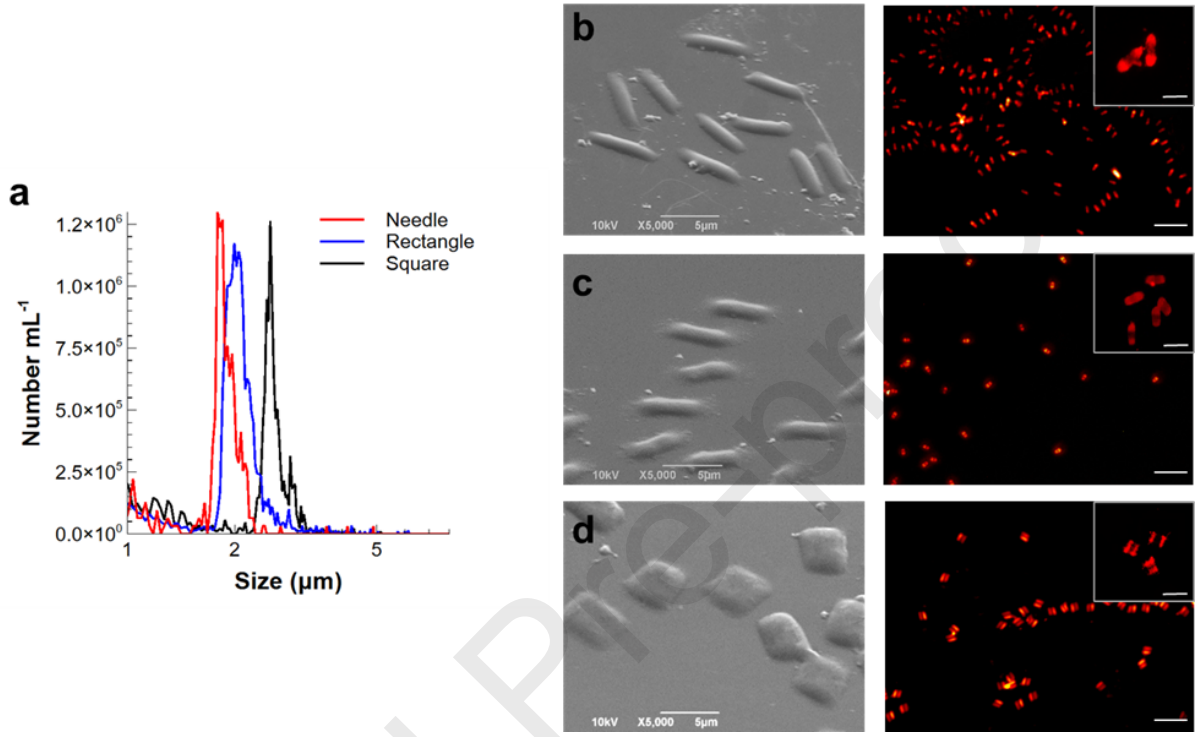

Figure 5: **MMH with different aspect ratios. a.** Multisizer analysis of three characteristic MMH geometries. **b-d.** SEM and fluorescence characterization of the needle, rectangle, and square geometries. Fluorescence image scale is 20 µm. The inset images show confocal images of the MMH, scale for the inset is 5 µm.

in the polymeric MMH. Depending on the application, these payloads could be imaging tracers (fluorescent molecule for optical imaging as per the RhB example, Gd^{3+}- or $^{64}Cu^{2+}$-ions for MR or Nuclear Imaging), therapeutic molecules and pro-drugs, and even nanoparticles and combination thereof. It should be here highlighted that 2PP is not limited by the solvent for particle fabrication like other template-based strategies, thus providing a flexible strategy to incorporate different cargos simultaneously into the MMH.

As RhB is representative of a small molecule, the next step was that of incorporating 200 nm red-fluorescent polystyrene beads (PS). These were uniformly dispersed in the working solution and entrapped within the MMH following photopolymerization, as schematically shown in **Figure 6a**. As documented by the red fluorescent coloration of **Figure 6b**, the MMH were loaded with the 200 nm polystyrene beads. A patchy fluorescent signal was observed via confocal microscopy throughout the MMH hydrogel structure resulting from the relatively large nature of the PS as compared to the molecular RhB (**Figure 5b-d**). As a second example, the hydrophobic green fluorescent molecule curcumin (CURC) was first encapsulated into PLGA-based spherical polymeric nanoparticles (CURC-SPN) (**Figure S7**)[32] and then added to the working solution. These 200 nm nanoparticles also were effectively entrapped in the MMH, as documented by the green, fluorescent coloration of the microparticles (**Figure 6c**). Finally, lipid nanoparticles were also loaded into MMH. The incorporation of the water dispersible lipid nanoparticles into MMH required some adjustment as compared to the original protocol. Specifically, the photoinitiator Lucirin TPO-L, insoluble in water, was substituted with the water-soluble lithium phenyl-2,4,6-trimethylbenzoylphosphinate (LAP) and the system was operated at 60 mW of laser power. Initially, lipid Cy5 containing liposomes were realized and loaded into MMH (**Figure S8**). Progressing to a more complex nano-formulation, a fluorescein amidite (FAM)-labelled oligonucleotide was loaded into lipid nanoparticles (oligo-LNP) by microfluidic mixing using a Nanoassemblr Benchtop.[33] These oligo-LNP were then loaded into the MMH as seen in **Figure 6d**. Orthogonal views of the z-stack images show the fluorecence distribution of the nanoparticles embedded within the MMH (**Figure S9**). Indeed, following the same method, multiple and different nano-formulations could be dispersed within the working solution and physically entrapped within the PEGDA matrix of the MMH upon polymerization. Thus, it has been demonstrated that the hierarchically structured MMH could be loaded with hydrophobic and hydrophilic therapeutic cargos, simultaneously. Note that for

simplicity the sole case of square MMH was considered, but the same strategy can be readily extended to any MMH geometry.

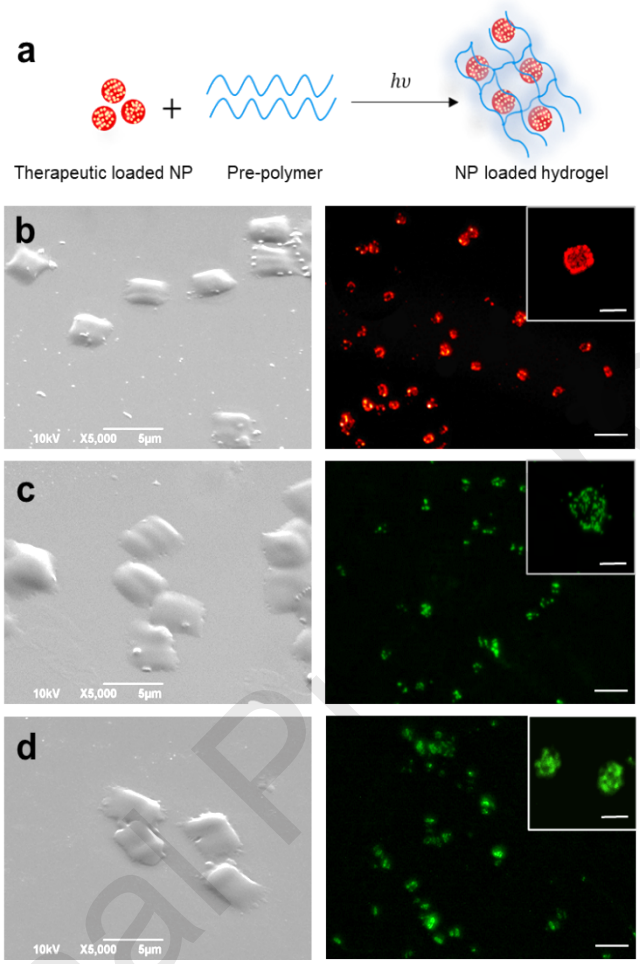

Figure 6: **Incorporating a payload into MMH. a.** Schematic depicting in situ loading of nanoparticles in MMH. **b-d.** SEM images and fluorescence microscopy images of 200 nm-PS beads, curcumin SPNs and ssRNA LNPs loaded square MMH, scale is 20 μm. The inset image is a confocal image of the MMH; scale for the inset is 5 μm.

Conclusion

Studies reporting 2PP for microparticle fabrication typically focus on 3D printing complex geometries using galvanometer mirrors[26] or digital micromirror devices[34] and some fabricate hydrogels in static droplets[35, 36] or on sacrificial templates.[37] In this study, the authors fabricated sub-10 μm free-floating PEGDA hydrogel microparticles (MMH)

continuously in a microfluidic device at maximum throughput of 60 particles per second, higher than other reports in this field.[26, 27] MMH of varying aspect ratios were fabricated simply by tuning four different process parameters: flow velocity Q, chopper frequency f, and the monomer C_{PEG} and photoinitiator C_{PI} concentrations. The effect of these parameters on the MMH size and shape was assessed experimentally. A computational model describing the reactive-convective-diffusion problem ruling the particle formation was developed and used to corroborate and interpret the experimental observation. It resulted that the particle length could be readily increased by reducing the fluid velocity, increasing the laser power and monomer/photoinitiator concentrations, while the particle width would grow quasi linearly with the fluid velocity and chopper frequency. Finally, it was demonstrated that a variety of therapeutic and imaging cargos, including small imaging and drug molecules, fragments of nucleic acids, polymeric and lipid nanoparticles can be readily entrapped within the MMH matrix originating hierarchical theranostic system. In this regard, most fabrication strategies for polymeric bio-mimicking microparticles have been limited by the substrate or the resolution.[13, 23, 25] This work is expected to trigger additional studies aiming at realizing MMH with more complex and defined geometries; utilizing different monomers, including hyaluronic acid, chitosan and other photopolymerizable monomers; and incorporating a multitude of cargos while using a simple two-photon microfluidic based fabrication set-up.

Acknowledgements

This project was partially supported by the European Union's Horizon 2020 research and innovation programme under the Marie Skłodowska-Curie grant agreement no. 754490 (MINDED) and the Fondazione Istituto Italiano di Tecnologia. The authors acknowledge the precious support provided by the Nikon Center, the Material Characterization Facility, the Electron Microscopy and Nanofabrication facilities at the Italian Institute of Technology. The authors would like to thank Dr. Michele Oneto, Dr. Marco Scotto and Dr. Salvatore Surdo for

their assistance with the optical setup. The authors would also like to thank Dr. Sayanti Brahmachari for meaningful discussions.

References

1. Kazi KM, Mandal AS, Biswas N, Guha A, Chatterjee S, Behera M, et al. Niosome: A future of targeted drug delivery systems. J Adv Pharm Technol Res. 2010;1(4):374-80.

2. Brannon-Peppas L, Blanchette JO. Nanoparticle and targeted systems for cancer therapy. Advanced Drug Delivery Reviews. 2004;56(11):1649-59.

3. Allen TM, Cullis PR. Liposomal drug delivery systems: From concept to clinical applications. Advanced Drug Delivery Reviews. 2013;65(1):36-48.

4. Touitou E, Godin B, Dayan N, Weiss C, Piliponsky A, Levi-Schaffer F. Intracellular delivery mediated by an ethosomal carrier. Biomaterials. 2001;22(22):3053-9.

5. Rao JP, Geckeler KE. Polymer nanoparticles: Preparation techniques and size-control parameters. Progress in Polymer Science. 2011;36(7):887-913.

6. Chen S, Cheng S-X, Zhuo R-X. Self-Assembly Strategy for the Preparation of Polymer-Based Nanoparticles for Drug and Gene Delivery. Macromolecular Bioscience. 2011;11(5):576-89.

7. Liu Y, Cheng C, Liu Y, Prud'homme RK, Fox RO. Mixing in a multi-inlet vortex mixer (MIVM) for flash nano-precipitation. Chemical Engineering Science. 2008;63(11):2829-42.

8. Lim J-M, Swami A, Gilson LM, Chopra S, Choi S, Wu J, et al. Ultra-High Throughput Synthesis of Nanoparticles with Homogeneous Size Distribution Using a Coaxial Turbulent Jet Mixer. ACS Nano. 2014;8(6):6056-65.

9. Kulkarni SA, Feng S-S. Effects of Particle Size and Surface Modification on Cellular Uptake and Biodistribution of Polymeric Nanoparticles for Drug Delivery. Pharmaceutical Research. 2013;30(10):2512-22.

10. Walkey CD, Olsen JB, Guo H, Emili A, Chan WCW. Nanoparticle Size and Surface Chemistry Determine Serum Protein Adsorption and Macrophage Uptake. Journal of the American Chemical Society. 2012;134(4):2139-47.

11. Kersey FR, Merkel TJ, Perry JL, Napier ME, DeSimone JM. Effect of Aspect Ratio and Deformability on Nanoparticle Extravasation through Nanopores. Langmuir. 2012;28(23):8773-81.

12. Champion JA, Mitragotri S. Role of target geometry in phagocytosis. Proc Natl Acad Sci U S A. 2006;103(13):4930-4.

13. Perry JL, Reuter KG, Kai MP, Herlihy KP, Jones SW, Luft JC, et al. PEGylated PRINT nanoparticles: the impact of PEG density on protein binding, macrophage association, biodistribution, and pharmacokinetics. Nano Lett. 2012;12(10):5304-10.

14. Merkel TJ, Jones SW, Herlihy KP, Kersey FR, Shields AR, Napier M, et al. Using mechanobiological mimicry of red blood cells to extend circulation times of hydrogel microparticles. Proceedings of the National Academy of Sciences. 2011;108(2):586.

15. Palomba R, Palange AL, Rizzuti IF, Ferreira M, Cervadoro A, Barbato MG, et al. Modulating Phagocytic Cell Sequestration by Tailoring Nanoconstruct Softness. ACS Nano. 2018;12(2):1433-44.

16. Lee T-R, Choi M, Kopacz AM, Yun S-H, Liu WK, Decuzzi P. On the near-wall accumulation of injectable particles in the microcirculation: smaller is not better. Sci Rep. 2013;3:2079.

17. Cooley M, Sarode A, Hoore M, Fedosov DA, Mitragotri S, Sen Gupta A. Influence of particle size and shape on their margination and wall-adhesion: implications in drug delivery vehicle design across nano-to-micro scale. Nanoscale. 2018;10(32):15350-64.

18. Ben-Akiva E, Meyer RA, Yu H, Smith JT, Pardoll DM, Green JJ. Biomimetic anisotropic polymeric nanoparticles coated with red blood cell membranes for enhanced circulation and toxin removal. Science Advances. 2020;6(16):eaay9035.

19. Colasuonno M, Palange AL, Aid R, Ferreira M, Mollica H, Palomba R, et al. Erythrocyte-Inspired Discoidal Polymeric Nanoconstructs Carrying Tissue Plasminogen Activator for the Enhanced Lysis of Blood Clots. ACS Nano. 2018;12(12):12224-37.

20. Palange AL, Palomba R, Rizzuti IF, Ferreira M, Decuzzi P. Deformable Discoidal Polymeric Nanoconstructs for the Precise Delivery of Therapeutic and Imaging Agents. Mol Ther. 2017;25(7):1514-21.

21. Acharya G, Shin CS, Vedantham K, McDermott M, Rish T, Hansen K, et al. A study of drug release from homogeneous PLGA microstructures. J Control Release. 2010;146(2):201-6.

22. Rolland JP, Maynor BW, Euliss LE, Exner AE, Denison GM, DeSimone JM. Direct Fabrication and Harvesting of Monodisperse, Shape-Specific Nanobiomaterials. Journal of the American Chemical Society. 2005;127(28):10096-100.

23. Champion JA, Katare YK, Mitragotri S. Making polymeric micro- and nanoparticles of complex shapes. Proceedings of the National Academy of Sciences. 2007;104(29):11901.

24. Buyukserin F, Aryal M, Gao J, Hu W. Fabrication of Polymeric Nanorods Using Bilayer Nanoimprint Lithography. Small. 2009;5(14):1632-6.

25. Dendukuri D, Pregibon DC, Collins J, Hatton TA, Doyle PS. Continuous-flow lithography for high-throughput microparticle synthesis. Nature Materials. 2006;5(5):365-9.

26. Shaw LA, Chizari S, Shusteff M, Naghsh-Nilchi H, Di Carlo D, Hopkins JB. Scanning two-photon continuous flow lithography for synthesis of high-resolution 3D microparticles. Opt Express. 2018;26(10):13543-8.

27. Chizari S, Udani S, Farzaneh A, Stoecklein D, Carlo DD, Hopkins JB. Scanning two-photon continuous flow lithography for the fabrication of multi-functional microparticles. Opt Express. 2020;28(26):40088-98.

28. Laza SC, Polo M, Neves AAR, Cingolani R, Camposeo A, Pisignano D. Two-Photon Continuous Flow Lithography. Advanced Materials. 2012;24(10):1304-8.

29. Uppal N, Shiakolas PS. Experiments and characterization of two photon polymerization using 1 kHz femtosecond laser system: SPIE; 2008.

30. Zhou X, Hou Y, Lin J. A review on the processing accuracy of two-photon polymerization. AIP Advances. 2015;5(3):030701.

31. Dendukuri D, Panda P, Haghgooie R, Kim JM, Hatton TA, Doyle PS. Modeling of Oxygen-Inhibited Free Radical Photopolymerization in a PDMS Microfluidic Device. Macromolecules. 2008;41(22):8547-56.

32. Ameruoso A, Palomba R, Palange AL, Cervadoro A, Lee A, Di Mascolo D, et al. Ameliorating Amyloid-β Fibrils Triggered Inflammation via Curcumin-Loaded Polymeric Nanoconstructs. Front Immunol. 2017;8:1411.

33. Belliveau NM, Huft J, Lin PJ, Chen S, Leung AK, Leaver TJ, et al. Microfluidic Synthesis of Highly Potent Limit-size Lipid Nanoparticles for In Vivo Delivery of siRNA. Mol Ther Nucleic Acids. 2012;1(8):e37.

34. Geng Q, Wang D, Chen P, Chen S-C. Ultrafast multi-focus 3-D nano-fabrication based on two-photon polymerization. Nature Communications. 2019;10(1):2179.

35. Baldacchini T, Snider S, Zadoyan R. Two-photon polymerization with variable repetition rate bursts of femtosecond laser pulses. Opt Express. 2012;20(28):29890-9.

36. Xing J, Liu L, Song X, Zhao Y, Zhang L, Dong X, et al. 3D hydrogels with high resolution fabricated by two-photon polymerization with sensitive water soluble initiators. Journal of Materials Chemistry B. 2015;3(43):8486-91.

37. Saraswat YC, Ibis F, Rossi L, Sasso L, Eral HB, Fanzio P. Shape anisotropic colloidal particle fabrication using 2-photon polymerization. Journal of Colloid and Interface Science. 2020;564:43-51.

38. Mendonca CR, Correa DS, Baldacchini T, Tayalia P, Mazur E. Two-photon absorption spectrum of the photoinitiator Lucirin TPO-L. Applied Physics A. 2008;90(4):633-6.

39. Kızılel S, Pérez-Luna VH, Teymour F. Mathematical Model for Surface-Initiated Photopolymerization of Poly(ethylene glycol) Diacrylate. Macromolecular Theory and Simulations. 2006;15(9):686-700.

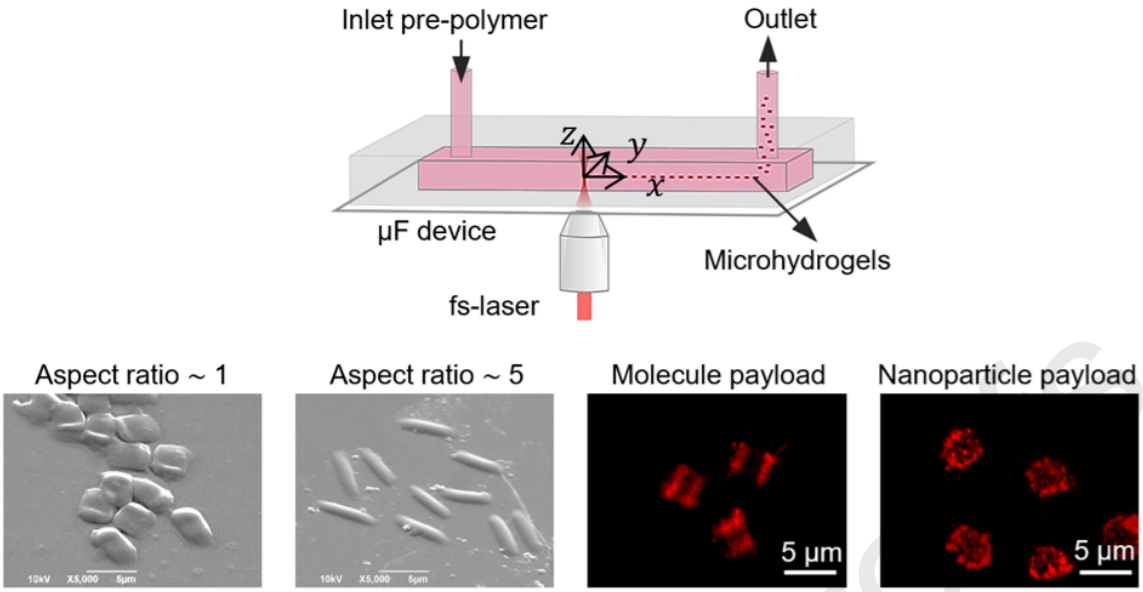

Declaration of interests

☒ The authors declare that they have no known competing financial interests or personal relationships that could have appeared to influence the work reported in this paper.

☐The authors declare the following financial interests/personal relationships which may be considered as potential competing interests:

Purnima N Manghnani: Conceptualization, Investigation, Validation, Formal Analysis and Writing-Original Draft

Valentina Di Francesco: Validation

Carlo Panella La Capria: Investigation and Validation

Michele Schlich: Validation

Marco Elvino Miali: Validation

Thomas Lee Moore: Validation

Alessandro Zunino: Formal Analysis

Marti Duocastella: Conceptualization, Supervision, Writing - Review & Editing

Paolo Decuzzi: Conceptualization, Supervision, Funding acquisition, Writing - Review & Editing